*land*

MDPI

*Article*

# Construction of a Joint Newmark–Runout Model for Seismic Landslide Risk Identification: A Case Study in the Eastern Tibetan Plateau

**Zhihua Yang [1], Yuming Wu [2,*], Changbao Guo [1] and Ximao Mai [1,3]**

[1] Institute of Geomechanics, Chinese Academy of Geological Sciences, Beijing 100081, China; yangzhihua@mail.cgs.gov.cn (Z.Y.); guochangbao@mail.cgs.gov.cn (C.G.); maiximaoyyds@cug.edu.cn (X.M.)
[2] Institute of Geographic Sciences and Natural Resources Research, Chinese Academy of Sciences, Beijing 100101, China
[3] Faculty of Engineering, China University of Geosciences, Wuhan 430074, China
* Correspondence: wuym@lreis.ac.cn

**Abstract:** The key to seismic landslide risk identification resides in the accurate evaluation of seismic landslide hazards. The traditional evaluation models for seismic landslide hazard seldom consider the landslide dynamic runout process, leading to an underestimation of seismic landslide hazard. Therefore, a joint Newmark–Runout model based on landslide dynamic runout is proposed. According to the evaluation results of static seismic landslide hazard, the landslide source points can be extracted, and the landslide dynamic runout process is simulated to obtain the dynamic seismic landslide hazard. Finally, the static and dynamic seismic landslide hazards are fused to obtain an optimized seismic landslide hazard. In September 2022, a strong Ms6.8 earthquake occurred in the eastern Tibetan Plateau, triggering thousands of landslides. Taking the 2022 Luding earthquake-induced landslide as a sample, the function relationship between seismic slope displacement and landslide occurrence probability is statistically modeled, which partly improves the traditional Newmark model. The optimized seismic landslide hazard evaluation of the Luding earthquake area is conducted, and then, the seismic landslide risk identification is completed by taking roads and buildings as hazard-affected bodies. The results show that the length of the roads facing very high and high seismic landslide risks are 3.36 km and 15.66 km, respectively, and the buildings on the Moxi platform near the epicenter are less vulnerable to seismic landslides. The research findings can furnish critical scientific and technological support for swift earthquake relief operations.

**Keywords:** seismic landslide; landslide hazard; landslide risk; joint Newmark–Runout model; Luding earthquake

check for updates

**Citation:** Yang, Z.; Wu, Y.; Guo, C.; Mai, X. Construction of a Joint Newmark–Runout Model for Seismic Landslide Risk Identification: A Case Study in the Eastern Tibetan Plateau. *Land* **2024**, *13*, 1832. https://doi.org/10.3390/land13111832

Academic Editor: Fabrizio Terenzio Gizzi

Received: 13 September 2024
Revised: 29 October 2024
Accepted: 29 October 2024
Published: 4 November 2024

**Copyright:** © 2024 by the authors. Licensee MDPI, Basel, Switzerland. This article is an open access article distributed under the terms and conditions of the Creative Commons Attribution (CC BY) license (https://creativecommons.org/licenses/by/4.0/).

## 1. Introduction

A seismic landslide is one of the severe geological hazards in complex mountainous and gorge areas. Strong earthquakes can trigger thousands of landslides, and these secondary disasters and their disaster chains associated with earthquakes can cause serious economic losses and casualties [1–3], even more than the loss caused by the earthquake itself [4]. The landslide activity period after a major earthquake may last for several decades [5]. Seismic landslide risk identification plays a crucial guiding role in timely earthquake relief and is an important research topic worthy of attention.

The key to seismic landslide risk identification lies in the accurate evaluation of seismic landslide hazards. Numerous mature mathematical models can be employed to conduct a seismic landslide hazard evaluation. At the monomer or small region scale, some analytical and simulation methods, such as pseudo-static analysis, the finite-element model, the finite-difference model, and the discrete-element model, can be employed to address slope stability and dynamic behavior under seismic motion [6,7]. At a regional scale, multiple models for

seismic landslide hazard evaluation and mapping have been established by analyzing seismic landslide distribution patterns and disaster-causing factor sensitivity, such as artificial neural network [8], support vector machine, Bayesian network [9], logistic regression analysis [10], analytical hierarchy process [11], and linear regression [12]. The Newmark model, based on cumulative slope displacement, was developed to calculate seismic landslide hazards [13,14]. Subsequently, based on substantial research results regarding the statistical characteristics of seismic landslides, the improved Newmark empirical prediction model [15,16] and statistical probability model [17,18] were presented. This simplified Newmark model is applicable and can efficiently perform seismic landslide hazard evaluation at a regional scale [19].

At a regional scale, the current models and methods can obtain the location where landslides may occur under the action of seismic motion but cannot obtain the runout path and accumulation body range after landslide instability, which reduces the influence range of seismic landslide and underestimates the seismic landslide hazard. Here, the evaluation results of seismic landslide hazard from traditional models can be called static seismic landslide hazard, and the influence of the dynamic runout process after landslide instability is called dynamic seismic landslide hazard. A joint program, combining the landslide probability model and the rock mass movement model, has been proposed [20], but the results of the two models have not been well integrated. To solve this problem and improve seismic landslide hazard accuracy, a joint Newmark–Runout model based on landslide source points and landslide dynamic runout is proposed, which integrates the static and dynamic seismic landslide hazard to obtain an optimized seismic landslide hazard.

In September 2022, a strong Ms6.8 earthquake in the eastern Tibetan Plateau induced thousands of landslides [21–25]. Some of the seismic landslides blocked rivers and formed barrier lakes, which had a serious impact on earthquake relief. Taking the Luding earthquake-induced landslide as a sample, the function relationship between landslide occurrence probability and seismic slope displacement is statistically modeled, which partly improves the traditional Newmark model. The proposed joint Newmark–Runout model is employed to evaluate the seismic landslide hazard in the Luding earthquake area, and the seismic landslide risk identification for roads and buildings is completed. The research method and findings offer critical scientific and technological support for swift earthquake relief operations and provide a significant reference for similar works of seismic landslide risk identification.

## 2. Methods and Materials

### *2.1. Joint Newmark–Runout Model*

To enhance the precision of seismic landslide hazard evaluation, a joint Newmark–Runout model is proposed (Figure 1). The fundamental steps to implement this model are as follows: (1) conduct a comprehensive field investigation in the earthquake-affected area to gather essential data, such as geological conditions and earthquake-induced landslides; (2) analyze the developmental characteristics and distribution patterns of these landslides; (3) perform a static seismic landslide hazard evaluation using traditional models and identify seismic landslide source points; (4) simulate the dynamic runout process after landslide instability based on identified landslide source points to derive dynamic seismic landslide hazard; (5) integrate both the static and dynamic seismic landslide hazards to formulate an optimized seismic landslide hazard; and (6) identify seismic landslide risk by taking roads and buildings as a hazard-affected body.

In this study, a simplified Newmark model grounded in statistical principles of many pieces of seismic landslide data is employed to obtain the static seismic landslide hazard. The natural breakpoint method is utilized to categorize the different levels of static seismic landslide hazard. The locations with very high and high seismic landslide hazards are identified as potential landslide source points. Additionally, the Rockfall model is used to simulate the dynamic movement process of rock masses after landslide instability, using the identified landslide source points as the input data for the Rockfall model (landslide source

area). Furthermore, the landslide dynamic runout parameters are leveraged to characterize the dynamic seismic landslide hazard.

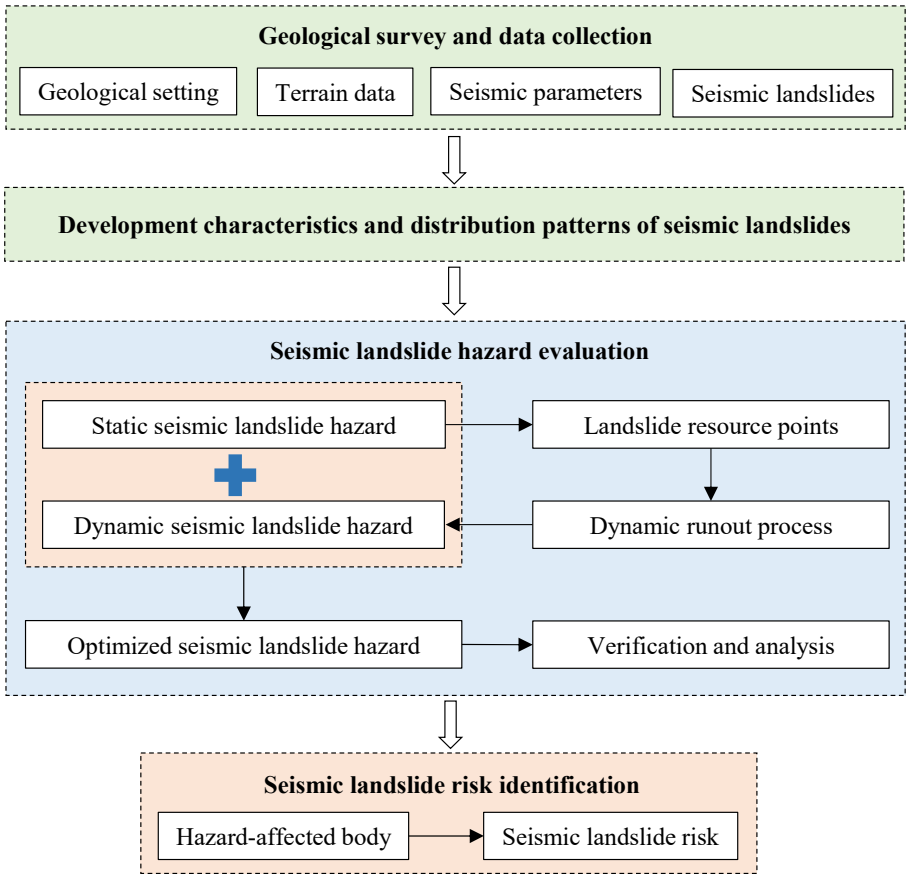


**Figure 1.** Flowchart of seismic landslide risk identification using the joint Newmark–Runout model.

### *2.2. Newmark Model*

The theoretical foundation of the traditional Newmark model is rooted in the limit equilibrium theory of infinite slopes [26]. When the external dynamic force exceeds the critical acceleration, the finite slope displacement will occur and continuously accumulate, resulting in permanent displacement [27,28]. The rigorous Newmark model, based on the seismic acceleration integral, is not suitable for calculating seismic slope displacement at a regional scale. Based on the universal statistical principles derived from a substantial number of seismic landslide samples, a simplified Newmark model was subsequently developed [14,29], whose calculation can be performed using a raster calculator tool and raster data format within a GIS platform.

The slope critical acceleration ($a_c$) is defined as the seismic motion acceleration at which the sliding force equals the anti-sliding force acting on the sliding bodies. The slope's critical acceleration can be determined using Equation (1) [13], where $g$ represents gravitational acceleration, $\alpha$ denotes sliding surface angle, and $F_s$ denotes the slope static safety factor. The slope static safety factor serves as an indicator of the stability of the slope body under non-dynamic loading and can be obtained using the slope stability formula (Equation (2)) [14,29]. In Equation (2), $c'$ denotes the effective internal cohesion, $\varphi'$ denotes the effective internal friction angle, $\gamma$ denotes the weight of the rock masses, $\gamma_w$ denotes the weight of the groundwater, $t$ denotes the depth of the sliding surface, $\alpha$ denotes the sliding surface angle, and $m$ denotes the thickness ratio of the saturated portion of the sliding body.

$$a_c = (F_s - 1)g \sin \alpha \quad (1)$$

$$F_s = \frac{c'}{\gamma t \sin\alpha} + \frac{\tan\varphi'}{\tan\alpha} - \frac{m\gamma_w \tan\varphi'}{\gamma \tan\alpha} = \frac{c'}{\gamma t \sin\alpha} + (1 - \frac{m\gamma_w}{\gamma}) \times \frac{\tan\varphi'}{\tan\alpha} \quad (2)$$

Upon determining the slope's critical acceleration, the statistical empirical relationship (Equation (3)) [30] is employed to calculate the seismic slope displacement ($D_n$), where *PGA* denotes the peak ground acceleration. The seismic slope displacement demonstrates a positive correlation with peak ground acceleration while exhibiting a negative correlation with slope critical acceleration. Ultimately, the landslide occurrence probability ($P$) will be determined using the statistical empirical relationship (Equation (4)) [30], which serves as an indicator of the seismic landslide hazard.

$$\lg D_n = 0.215 + \lg\left[\left(1 - \frac{a_c}{PGA}\right)^{2.341}\left(\frac{a_c}{PGA}\right)^{-1.438}\right] \quad (3)$$

$$P = m\left[1 - \exp(-aD_n^b)\right] \quad (4)$$

### 2.3. Rockfall Model

As a three-dimensional solid motion model, the Rockfall model can effectively handle substantial geospatial data pertinent to the behaviors of rock mass movement, such as frequency, energy, velocity, and trajectory [20,31]. The Rockfall model comprises two primary components, namely (1) simulations of rock mass movement, and (2) continuous raster surface modeling to represent the spatial distribution of rock mass trajectories [32]. The rock mass trajectory constitutes a fundamental aspect of the Rockfall model, employing the widely utilized "lumped mass" approach to simulate rock mass movement processes while disregarding the effect of rock mass shape. The trajectory of falling rock mass is calculated using a parabolic equation, defined as Equation (5). In Equation (5), $g$ represents gravitational acceleration, $t$ denotes time, $X_0$, $Y_{0,}$ and $Z_0$ denote the coordinates of the initial position of the rock mass, and $V_{x0}$, $V_{y0}$, and $V_{z0}$ indicate the initial velocities in the x, y, and z directions, respectively [20,31]. The Rockfall model incorporates dynamic processes based on a cell plane, making it particularly suitable for the spatially distributed analysis of geo-hazards [20]. The necessary input parameters encompass initial seeder characteristics, material composition properties, and topographic features, including the digital elevation model.

$$s = \begin{bmatrix} 0 \\ 0 \\ -\frac{1}{2}gt^2 \end{bmatrix} + \begin{bmatrix} V_{x0} \\ V_{y0} \\ V_{z0} \end{bmatrix} t + \begin{bmatrix} X_0 \\ Y_0 \\ Z_0 \end{bmatrix} \quad (5)$$

### 2.4. Materials

In response to the requirements for seismic landslide hazard evaluation and risk identification, the relevant data from the Luding earthquake area were collected and organized. Field investigations and low-altitude UAV flights were conducted in 2022 to obtain photographs and orthophoto images of typical earthquake-induced landslides. The orthophoto images and DSM data within the Luding earthquake area come from the Mountain Science Data Center (https://www.msdc.ac.cn/#/, accessed on 7 September 2022). The seismic landslide catalog of the Luding earthquake comes from free shared data (https://link.springer.com/article/10.1007/s11629-022-7772-0, accessed on 28 March 2023 [23], https://doi.org/10.1016/j.eqrea.2022.100181, accessed on 1 January 2023 [22]). The attribute parameters of the Luding earthquake, including the focal mechanism, are sourced from the National Earthquake Data Center (https://data.earthquake.cn/index.html, accessed on 7 September 2022). The peak ground acceleration of the Luding earthquake comes from the published literature [33]. The stratigraphic lithology and active fault data are derived from 1:200,000 geological maps (http://dcc.cgs.gov.cn/, accessed on 7 September 2022). The digital elevation model (DEM) utilizes the ARSTER GDEM (https://search.asf.alaska.edu/#/, accessed on 7 September 2022), allowing for the calculation of the slope angle and the terrain shadow based on the DEM. The road and building data are obtained through remote

sensing interpretation and utilizing remote sensing images from Google Earth. All vector data are converted to the raster format for computational purposes, with a resolution of 30 m.

## 3. Seismic Landslide Hazard Evaluation

### *3.1. Geological Setting*

On 5 September 2022, a significant Ms6.8 earthquake struck Luding County, Sichuan Province, China (Figure 2), with an epicenter at E 102.08°, N 29.59°, and a focal depth of 16 km. The maximum peak ground acceleration recorded is 0.42 g, accompanied by a maximum seismic intensity of IX degrees (Figure 3). The Luding earthquake is situated at the Y-shaped intersection of several active fault zones, including the Longmenshan fault, the Xianshuihe fault, the Daduhe fault, and the Anninghe fault on the eastern margin of the Qinghai–Tibet Plateau, an area characterized by strong tectonic activity and a high frequency of strong earthquakes [34]. The seismogenic fault associated with the Luding earthquake is the Moxi fault, located in the southern section of the Xianshuihe fault.

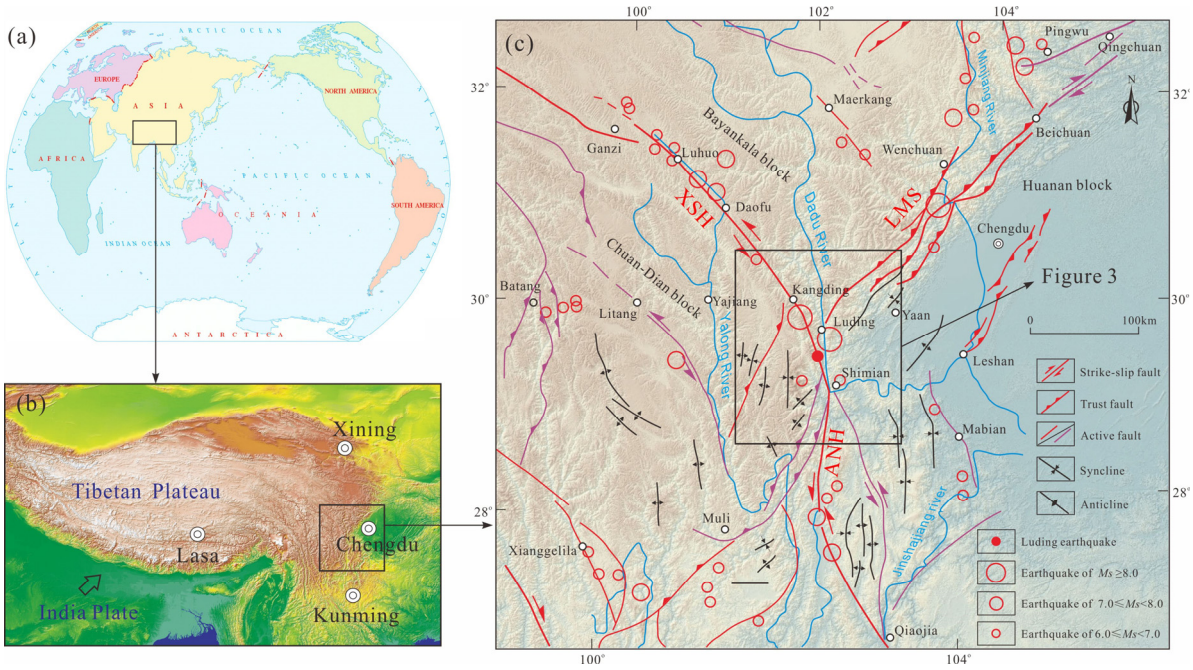


**Figure 2.** (**a**) The location of the Tibetan Plateau. (**b**) A general view of the Tibetan Plateau. (**c**) The major active structures in the eastern Tibetan Plateau and the geographical location of the 2022 Ms6.8 Luding earthquake. XSH indicates the Xianshuihe fault, ANH indicates the Anninghe fault, and LMS indicates the Longmenshan fault. The black rectangular box in Figure 2c indicates the scope of Figure 3.

The Xianshuihe fault is a prominent left-lateral strike–slip fault system characterized by significant Holocene activity and an overall northwest trend, exhibiting a history of strong seismic events, including 17 earthquakes exceeding Ms6.0 since 1725 and 8 earthquakes exceeding Ms7.0. The overall strike–slip rate of the Xianshuihe fault since the late Quaternary is approximately 10 mm/a [35], with a discernible increasing trend from the northwest section to the southeast section [36,37]. Furthermore, the earthquake occurrence within the Xianshuihe fault zone has exhibited a notable shift towards the southeast in recent years [38,39]. The Moxi fault has been characterized by left-lateral strike–slip movement since the late Quaternary, accompanied by vertical displacement components. The strike–slip rate is estimated to be 9.3–13.4 mm/a, while the vertical movement rate is estimated to be 1.5–3.2 mm/a, exhibiting distinct fault traces [40]. According to a focal mechanism analysis, the Luding earthquake is characterized as a high-dip left-lateral strike–slip event of the main aftershock type [21,24],

and the aftershocks are distributed in an NNW direction, among which 6486 aftershocks have been recorded, including 18 aftershocks of a magnitude of Ms3.0 and above.

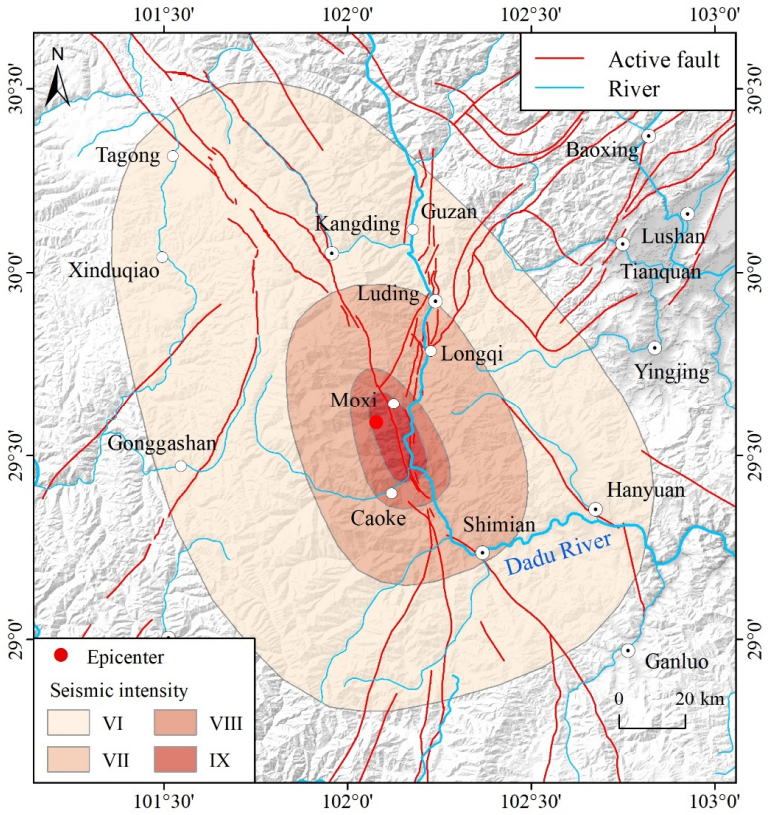


**Figure 3.** Seismic intensity and epicenter of the 2022 Ms6.8 Luding earthquake. Seismic intensity data come from http://www.mem.gov.cn/xw/yjglbgzdt/202209/t20220911_422190.shtml, accessed on 11 September 2022, which was determined based on the degree of seismic impact on the ground and buildings, as well as the Chinese seismic intensity scale (GB/T 17742-2020) [41].

The Luding earthquake is situated in the transition zone between the Sichuan Basin and the West Sichuan Plateau, characterized by a medium-alpine and erosional landform [24,36]. The geological tectonics and slope structure on both banks of the deep valley of the Dadu River are extremely complex. According to 1:200,000 geological maps, the granite, diorite, and other magmatic rocks are extensively exposed in the Luding earthquake area, accompanied by a significant presence of glacial deposits and Quaternary colluvial sediments. The average annual precipitation is approximately 664.4 mm [25].

### *3.2. Seismic Landslide Characteristics*

The landslide catalog serves as a critical dataset for investigating the characteristics of landslide development and distribution. The Ms6.8 Luding earthquake triggered thousands of landslides. Currently, several landslide catalogs induced by the Luding earthquake have been compiled through multi-source remote-sensing interpretation and field surveys. Among these, two landslide catalogs are available for public download, containing 5007 [22] and 8685 [23] landslides, respectively (Figure 4a). The second landslide catalog is used for this research. A statistical analysis indicates that the total area of the landslides induced by the Luding earthquake is approximately 30.66 $km^2$, and the largest landslide area is about 39.25 $\times$ $10^4$ $m^2$. There are 8665 landslides with an area smaller than 10 $\times$ $10^4$ $m^2$ and 8000 landslides with an area smaller than 1 $\times$ $10^4$ $m^2$. In general, the landslide number is large, but their scale is small. And they are predominantly distributed in regions with a seismic intensity of VII or higher.

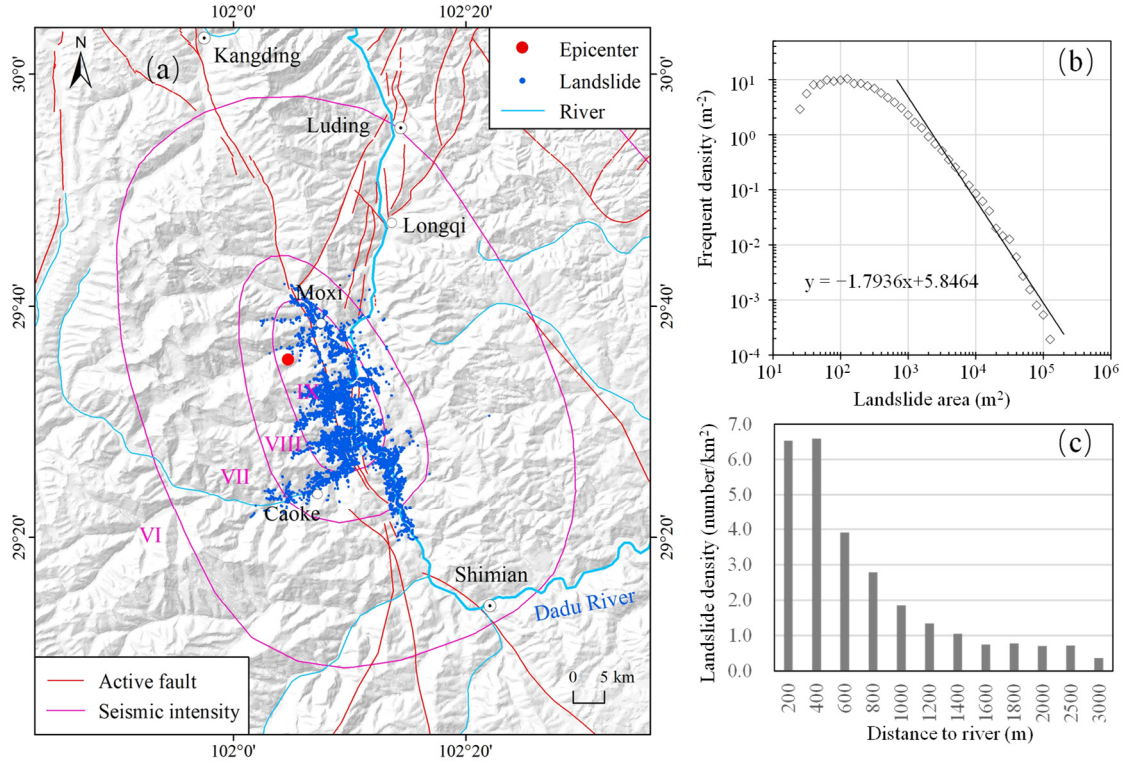


**Figure 4.** Characteristics of landslide development induced by the 2022 Ms6.8 Luding earthquake. (**a**) Spatial distribution of landslides (the landslide catalog comes from [23]). (**b**) Statistical correlation between landslide area and frequency density. (**c**) Statistical correlation between landslide distribution and river gully morphology.

The Luding earthquake-induced landslides exhibit a pronounced group effect, characterized by a clustered distribution on the southeast side of the epicenter, along both banks of the Dadu River, and on the west side of the Moxi fault [42]. In addition, the Luding earthquake-induced landslides are significantly controlled by active faults, topography, lithology, and river gully [21,23]. For example, the Luding earthquake-induced landslide was mainly developed within 400 m on both sides of the river gully (Figure 4c). The statistical relationship between the landslide area and the frequency density distribution (Figure 4b) indicates that the landslide area with the highest frequency density is approximately 90–110 $m^2$, while the frequency density exhibits an exponential decline as the landslide area increases. Many shallow landslides mainly developed in the Quaternary deposits and shallow strongly weathered rock masses (Figure 5), and many landslides evolved into landslide-debris flow. For instance, the disaster chain involves high-level landslide-debris flow-blocking rivers in alpine canyon regions, such as the Wandong River (Figure 5d).

### *3.3. Seismic Landslide Hazard*

#### 3.3.1. Static Seismic Landslide Hazard

The Luding earthquake-induced landslides are predominantly located in regions with a seismic intensity of VII and higher, which is designated as the primary study area. A simplified Newmark model, grounded in universal statistical principles, is adopted to perform a static seismic landslide hazard evaluation. The engineering geological units within the study area were classified into 12 categories (Figure 6, Table 1), each exhibiting varying susceptibility to landslide occurrence. The geological strata with similar geological ages, lithology, geological structures, and soil and rock properties are grouped into an engineering geological unit.

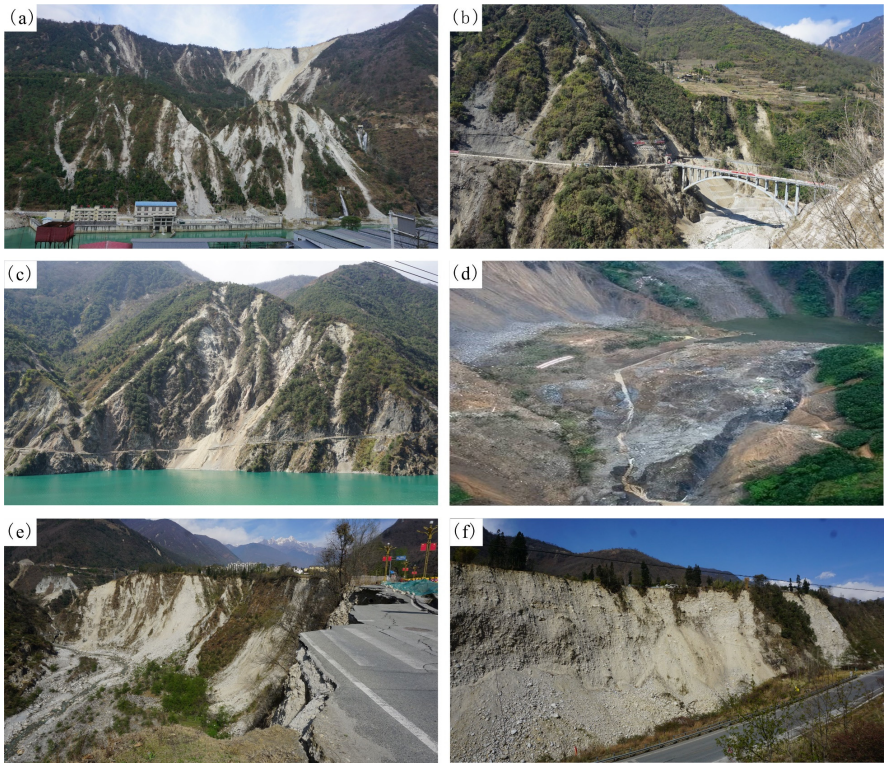


**Figure 5.** Representative landslides induced by the 2022 Ms6.8 Luding earthquake. (**a**) Deformation and failure of the old Mogangling landslide body on the right bank of the Dadu River. (**b**) Qinggangping landslide in the Hailuo gully. (**c**) Xinhuancun landslide in Detuo Town. (**d**) Landslide barrier lake in the Wandong River, a tributary on the right bank of the Dadu River. (**e**) Moraine landslide on the southwest side of the Moxi platform. (**f**) Moraine landslide on the northeast side of the Moxi platform. The photos of (**a**–**c**,**e**,**f**) come from field survey in 2022 conducted by the author of this paper. The photo (**d**) comes from field survey in 2022 conducted by other experts.

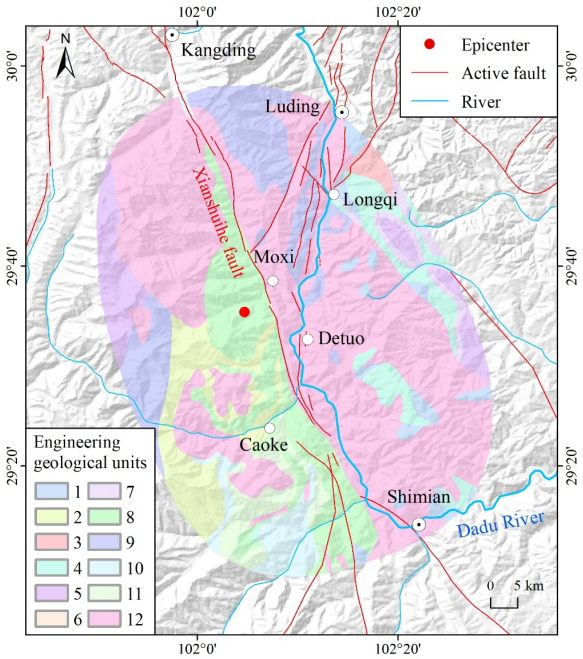


**Figure 6.** Engineering geological units within the Luding earthquake area. The properties of engineering geological units are detailed in Table 1.

**Table 1.** Property parameters of engineering geological units within the Luding earthquake area.

| ID | Engineering Geological Unit | $c'$/(kPa) | $\varphi'$/(°) | $\gamma$/(kN/m$^3$) |
|---|---|---|---|---|
| 1 | Hard thick-bedded sandstone | 26 | 33 | 26 |
| 2 | Moderately hard-to-hard, medium-to-thick-bedded sandstone with interbedded conglomerate, mudstone, and slate | 25 | 32 | 25 |
| 3 | Alternating layers of soft and hard medium-to-thick-bedded sandstone and mudstone with interbedded limestone | 23 | 30 | 24 |
| 4 | Soft to moderately hard, thin-to-medium-thick-bedded sandstone and mudstone | 22 | 28 | 23 |
| 5 | Soft thin-bedded mudstone and shale | 20 | 27 | 21 |
| 6 | Hard, medium-to-thick-bedded limestone and dolomite | 24 | 31 | 25 |
| 7 | Moderately hard, thin-to-medium-thick-bedded limestone and argillaceous limestone | 23 | 30 | 24 |
| 8 | Alternating layers of soft and hard medium-to-thick-bedded limestone and dolomite with interbedded sandstone and mudstone | 22 | 29 | 23 |
| 9 | Moderately hard-to-hard, thin-to-medium-thick bedded slate, phyllite, and metamorphic sandstone | 21 | 28 | 22 |
| 10 | Soft-to-moderately hard, thin-to-medium-thick bedded phyllite and schist with interbedded limestone, sandstone, and volcanic rocks | 20 | 26 | 21 |
| 11 | Hard blocky basalt | 27 | 34 | 29 |
| 12 | Hard blocky granite, andesite, and diorite | 26 | 33 | 28 |

Note: ID refers to the corresponding identification number of engineering geological units presented in Figure 6, $c'$ denotes effective internal cohesion, $\varphi'$ denotes effective internal friction angle, and $\gamma$ denotes weight of rock masses.

Based on the *Engineering Geology Handbook of China* [43], Standard for Engineering Classification of Rock Mass of China (GB/T 50218-2014) [44], and the relevant literature [45], the property parameters of engineering geological units can be preliminarily assigned. In addition, the weight of groundwater ($\gamma_w$) was 10 kN/m$^3$. The thickness ratio of the saturated portion of the sliding body (m) was 0.3, and the sliding surface angle ($\alpha$) corresponded to the topographic slope angle. The depth of the potential sliding surface (t) was established at 5, 4, 3, and 2 m for slopes with gradients of less than 30°, between 30° and 45°, between 45° and 60°, and greater than 60°, respectively [20]. First, the calculation of the slope static safety factor in the Luding earthquake area was conducted. During the iterative calculation, the initial parameters of engineering geological units were adjusted to ensure that the slope static safety factor exceeds one without seismic dynamic loading [39] while maintaining a minimum parameter value of 1.01 [29]. The final property parameters are shown in Table 1. Subsequently, the slope critical acceleration in the Luding earthquake area can be calculated successively (Figure 7). When compared with previous research findings, the resulting value range is deemed to be reasonable [29,39,45]. Regions characterized by lower slope critical acceleration exhibit a higher susceptibility to landslide occurrences.

Following the Luding earthquake, the spatial distribution of peak ground acceleration (PGA) was derived using a random finite-fault simulation method, based on monitoring data from nine seismic stations located within 100 km of the epicenter [33] (Figure 8). The simulated maximum peak ground acceleration reaches 0.42 g, occurring to the east of the epicenter and influenced by the seismogenic fault. The slope displacement under seismic dynamic action was computed using both slope critical acceleration and the peak ground acceleration within the Luding earthquake area.

Slope displacement does not necessarily indicate the occurrence of a significant landslide event. It is only when the slope displacement accumulates to a critical threshold that the slope masses may lose stability and slide along the failure surface, resulting in a landslide event [29]. The statistical functional relationship between seismic slope displacement and landslide occurrence probability can be represented by Equation (4) [29], utilizing the Weibull equation, where a, b, and m denote the coefficients of the equation.

The landslide occurrence probability is associated with the quantity and spatial distribution characteristics of seismic landslides. A higher number and density of seismic landslides correspond to an increased landslide occurrence probability.

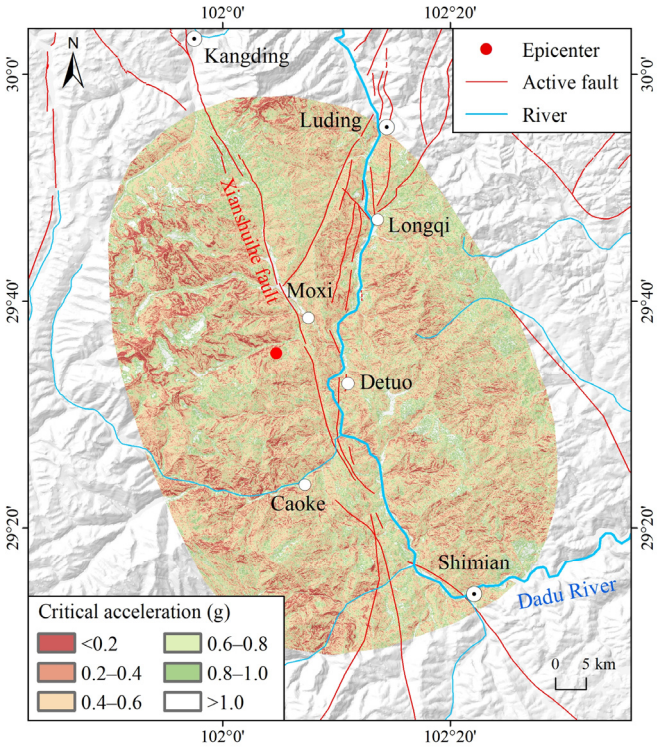


**Figure 7.** Slope critical acceleration within the Luding earthquake area.

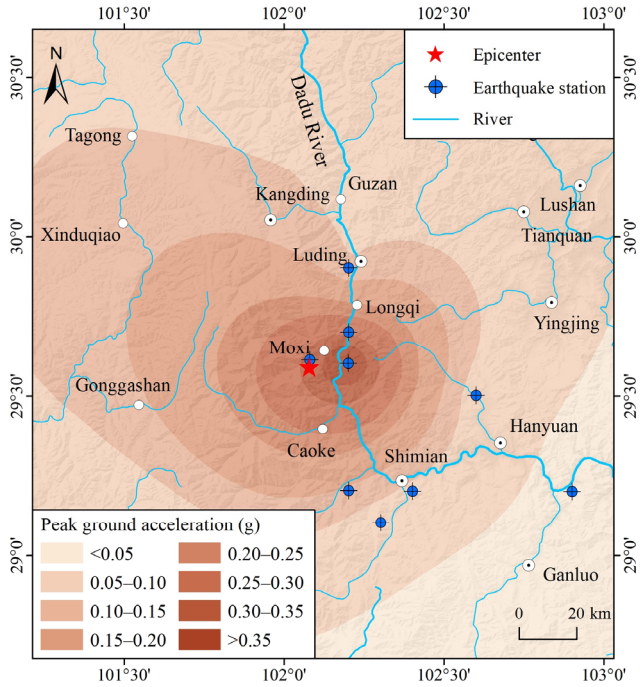


**Figure 8.** Seismic peak ground acceleration (PGA) within the Luding earthquake area [33].

The landslide samples within the Luding earthquake area are used to correct the equation coefficients to better adapt to the local seismic geological setting. The calculation steps can be succinctly summarized as follows. (1) Segment the seismic slope displacement

into ascending intervals, which will be represented on the horizontal axis and (2) calculate the regional area and landslide area within each seismic slope displacement interval, along with their ratio, which serves as an indicator of landslide occurrence probability on the vertical axis (Figure 9). Here, the calculation of the coverage area is based on the 30 m raster data, which cannot express the fine details of the landslide distribution, so the calculated landslide area may have a reduced error, which leads to the conservative result of the final landslide occurrence probability. (3) The regression analysis method is used to establish the functional equation (Equation (6)), with the seismic slope displacement serving as the independent variable.

$$P = 0.2698\left[1 - \exp(-0.0005D_n^{3.3776})\right] \quad (6)$$

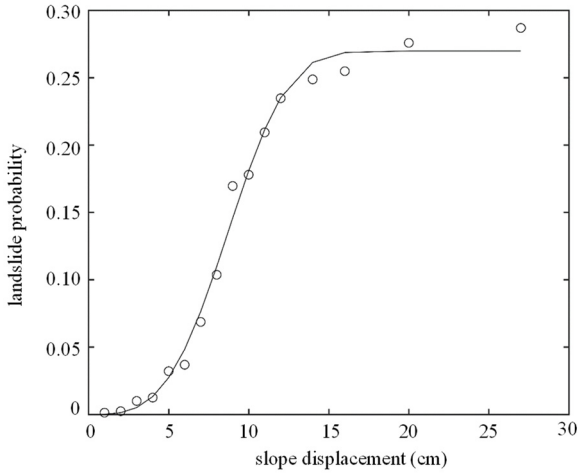


**Figure 9.** Relationship between seismic slope displacement and landslide occurrence probability within the Luding earthquake area.

The newly corrected functional equation (Equation (6)) was utilized to calculate the landslide occurrence probability within the Luding earthquake area. Equation (6) indicates that the landslide occurrence probability ranges from 0 to 0.2698. There are no clear standards or regulations for landslide hazard classification indicators. Generally, a quantitative and qualitative approach is used to classify landslide hazard levels. The natural breakpoint method is a classification technique based on numerical distribution law, aimed at maximizing the differentiation between classes. First, the landslide occurrence probability value was classified into five classes using the natural breakpoint method on the ArcGIS 10.8 platform as 0.1937–0.2680, 0.1426–0.1937, 0.0573–0.1426, 0.0135–0.0573, and 0–0.0135. Subsequently, based on the existing experience and the regional landslide development characteristics, the landslide occurrence probability classes have been adjusted to $\geq$0.20, 0.15–0.20, 0.05–0.15, 0.01–0.05, and <0.01, thereby representing static seismic landslide hazard levels as very high, high, moderate, low, and very low (Figure 10).

### 3.3.2. Dynamic Seismic Landslide Hazard

Grid elements with very high and high static seismic landslide hazards were extracted as potential landslide source points, as they are the most prone to instability and long runout distance. Here, the study scale is of a regional extent, not individual landslides, so the common default values of the Rockfall model are adopted for the surface parameters. That is, the normal restitution coefficient is 0.5, the tangential restitution coefficient is 0.8, and the friction angle is 20°. The parameters of the rock masses at landslide source points are derived from the property parameters of the engineering geological units presented in Table 1. Each grid element within the landslide source points was regarded as a landslide seeder, for which a potential movement direction was set according to the slope direction.

The displacement for each landslide seeder from the simulated seismic slope displacement was used as the initial displacement parameter. Based on the above parameters and the Rockfall model, the trajectory lines of rock mass movement after seismic landslide occurrence were calculated (Figure 11). Detailed instructions for the Rockfall model can be found in software manuals and related references [31,32].

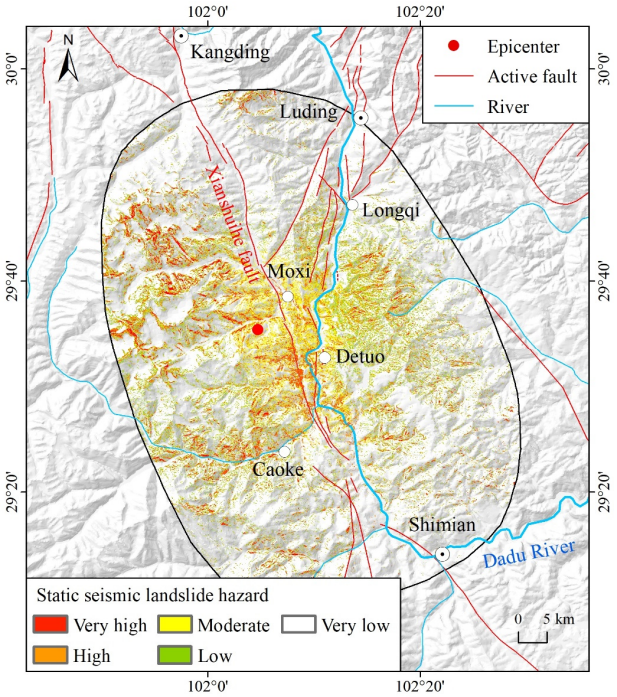


**Figure 10.** Spatial distribution of static seismic landslide hazard within the Luding earthquake area.

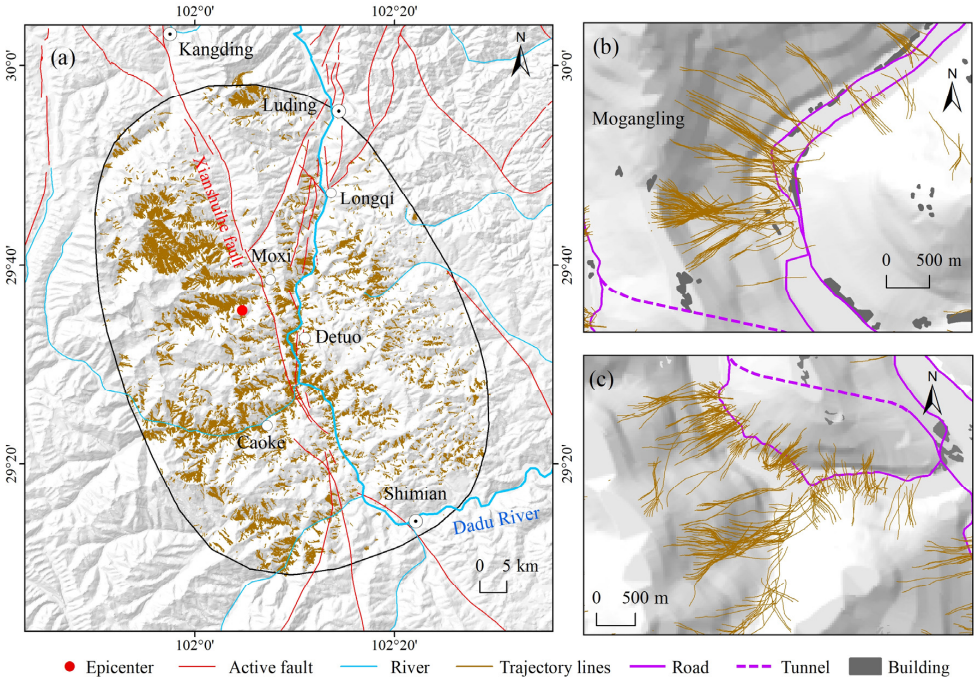


**Figure 11.** (**a**) The spatial distribution of the trajectory lines of rock mass movement after seismic landslide occurrence within the Luding earthquake area. (**b**) The trajectory lines of rock mass movement within the Mogangling area. (**c**) The trajectory lines of rock mass movement within the Moxi area.

Based on the trajectory lines of rock mass movement, the spatial frequency of moving rock masses can be calculated using the line density method on the ArcGIS platform. The more trajectory lines that pass through a certain location, the higher the spatial frequency of moving rock masses at this location, indicating that the landslide hazard at this location is greater. Subsequently, a neighborhood mean focal analysis (3 × 3 elements) was conducted to generate a continuous prediction surface for the spatial frequency of moving rock masses [20,31]. The natural breakpoint method was utilized to classify the spatial frequency of moving rock masses into five levels, which correspond to the five levels of dynamic seismic landslide hazard as very high, high, moderate, low, and very low (Figure 12).

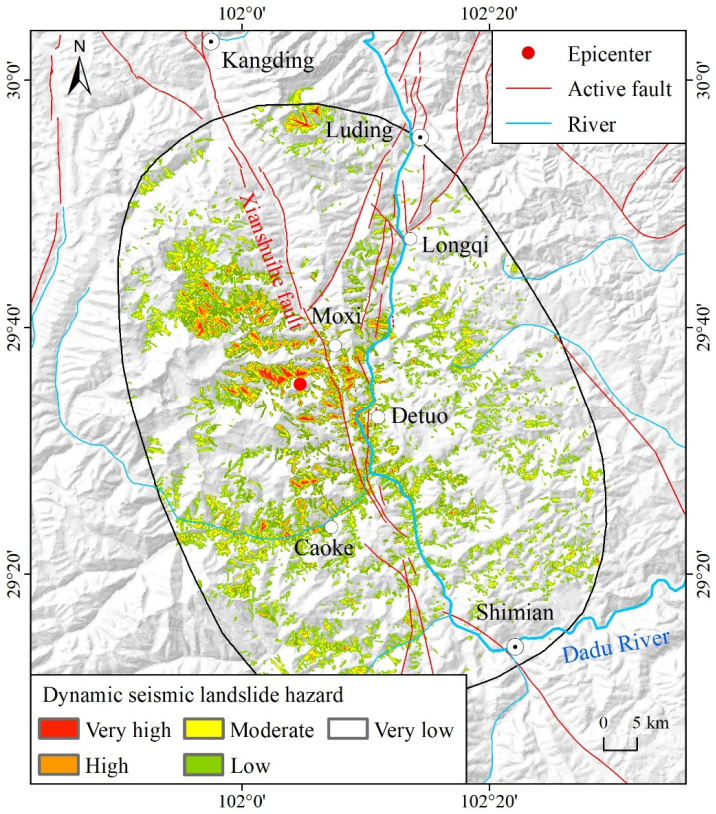


**Figure 12.** Spatial distribution of dynamic seismic landslide hazard within the Luding earthquake area.

### 3.3.3. Optimized Seismic Landslide Hazard

The static and dynamic seismic landslide hazard indexes have the characteristic of data heterogeneity. First, the static and dynamic seismic landslide hazard indexes were normalized using the min–max normalization method (Equation (7)). Subsequently, the two normalized indexes are fused together to derive a comprehensive seismic landslide hazard index using the factor overlay method via the ArcGIS raster calculator. The weights of both layers are set to 0.5. The comprehensive seismic landslide hazard index is classified into five levels, using the natural breakpoint method, that correspond to the five levels of optimized seismic landslide hazard as very high, high, moderate, low, and very low (Figure 13).

$$x = (x - x_{\min})/(x_{\max} - x_{\min}) \quad (7)$$

The ROC (receiver operating characteristic) curve method is utilized to verify the evaluation results of seismic landslide hazards. The AUC (area under curve) is utilized to characterize the model accuracy and has been widely applied in verifying regional landslide hazard evaluation [8]. It is widely accepted that the closer the AUC approaches one, the greater the model accuracy. An AUC value between 0.5 and 0.7 indicates poor

model accuracy, and an AUC value between 0.7 and 0.9 indicates good model accuracy. An AUC value exceeding 0.9 reflects excellent model accuracy.

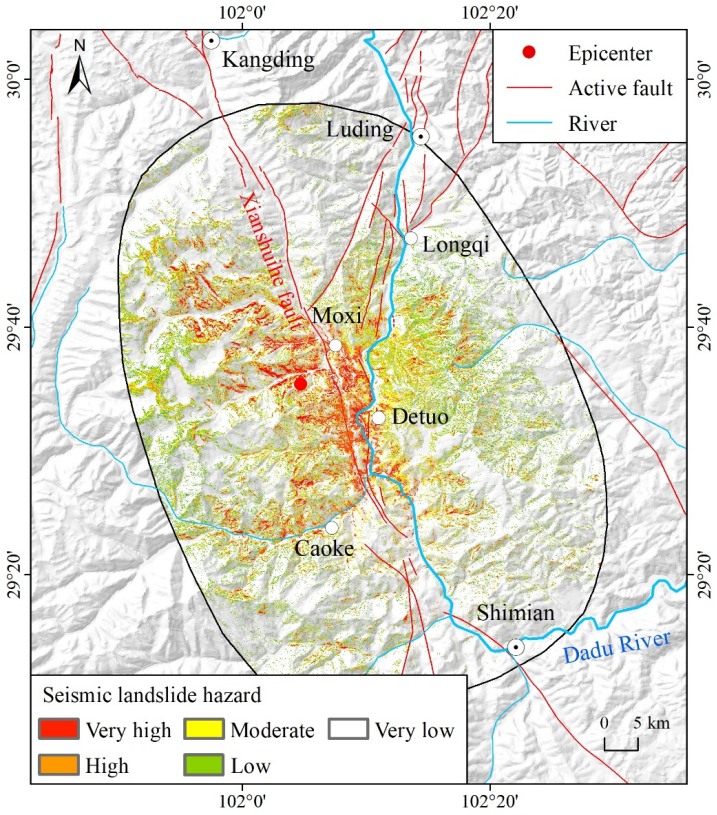


**Figure 13.** Spatial distribution of optimized seismic landslide hazard within the Luding earthquake area.

Taking the Luding earthquake-induced landslides as the validation samples [23], the relationship between seismic landslide hazard and landslide spatial distribution was subjected to statistical analysis. No matter how detailed the landslide interpretation and investigation, it cannot fully represent the actual landslide distribution. So far, the landslide inventory we have adopted for the Luding earthquake is the most comprehensive, with 8685 landslides. Statistical analysis shows that the landslide distribution characteristics conform to the general laws of seismic landslides [23], so it is sufficient as a validation sample for landslide hazards. The seismic landslide hazard was ranked in descending order and subsequently divided into equal intervals. The area accumulation percentage for each seismic landslide hazard interval (represented on the horizontal axis) and the corresponding landslide area accumulation percentage (represented on the vertical axis) were calculated, leading to the plotting of the ROC curve (Figure 14). The AUC values of the static and optimized landslide hazard evaluation results are 0.81 and 0.86, respectively, indicating that the proposed joint Newmark–Runout model effectively improves the precision of the seismic landslide hazard.

The spatial distribution characteristics of the seismic landslide hazard in areas with a seismic intensity of VII and above were statistically analyzed. The total area is 4380 km$^2$, with areas classified as having very high and high seismic landslide hazards covering 265 km$^2$, accounting for 6.05%. These areas are primarily concentrated in the southern gullies near the epicenter, along both sides of the Moxi fault, and on both banks of the Dadu River. The seismic landslide hazard exhibits spatial distribution characteristics similar to those of co-seismic landslides, characterized by a concentrated distribution along the Xianshuihe fault, a close relationship with seismic intensity, and significant influence from topography and geomorphology.

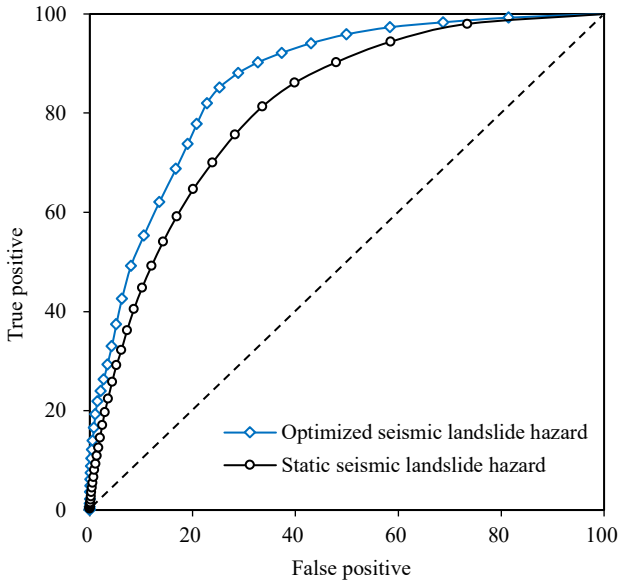


**Figure 14.** ROC curve illustrating the evaluation results of seismic landslide hazard within the Luding earthquake area.

## 4. Seismic Landslide Risk Identification

In the process of earthquake relief and emergency rescue, the degree of road accessibility and the extent of building damage are of paramount importance. Using remote-sensing interpretation and remote-sensing image data (19 March 2021 and 10 September 2022) from Google Earth, the road lines and building locations in the Luding earthquake area are identified. The linear road data includes both surface roads and tunnels. Tunnel interiors are not threatened by seismic landslides, so they are not included in the seismic landslide risk calculation. Utilizing the optimized seismic landslide hazard evaluation results, the linear road data within the Luding earthquake area were overlaid to assess the seismic landslide risks posed to roads. The optimized seismic landslide hazard data is in a grid format with a resolution of 30 m, and the road data is in linear vector format. Therefore, the seismic landslide risk posed to roads obtained by overlaying the grid and vector data has a precision of 30 m along the road direction.

The seismic landslide risks posed to roads were classified into five levels, namely very high, high, moderate, low, and very low (Figure 15, Table 2). The total length of the main roads in areas with a seismic intensity of VII and above is approximately 513.03 km, of which the lengths of roads classified as having very high and high seismic landslide risk are 3.36 km and 15.66 km, accounting for 0.66% and 3.05%, respectively. The length of roads with moderate seismic landslide risk is 43.04 km, accounting for 8.39%. The above roads are mainly distributed between Moxi Town and Caoke Town. The lengths of roads with low and very low seismic landslide risk are 82.30 km and 368.66 km, accounting for 16.04% and 71.86%, respectively, which are primarily located to the north of Moxi Town and to the south of Caoke Town. The total length of tunnels is about 19.31 km, except for entrances and exits, which are less affected by the seismic landslide.

**Table 2.** Statistics of seismic landslide risk posed to roads within the Luding earthquake area.

| Landslide Risk | Road Length (km) | Road Ratio (%) |
|---|---|---|
| very low | 368.66 | 71.86 |
| low | 82.30 | 16.04 |
| moderate | 43.04 | 8.39 |
| high | 15.66 | 3.05 |
| very high | 3.36 | 0.66 |

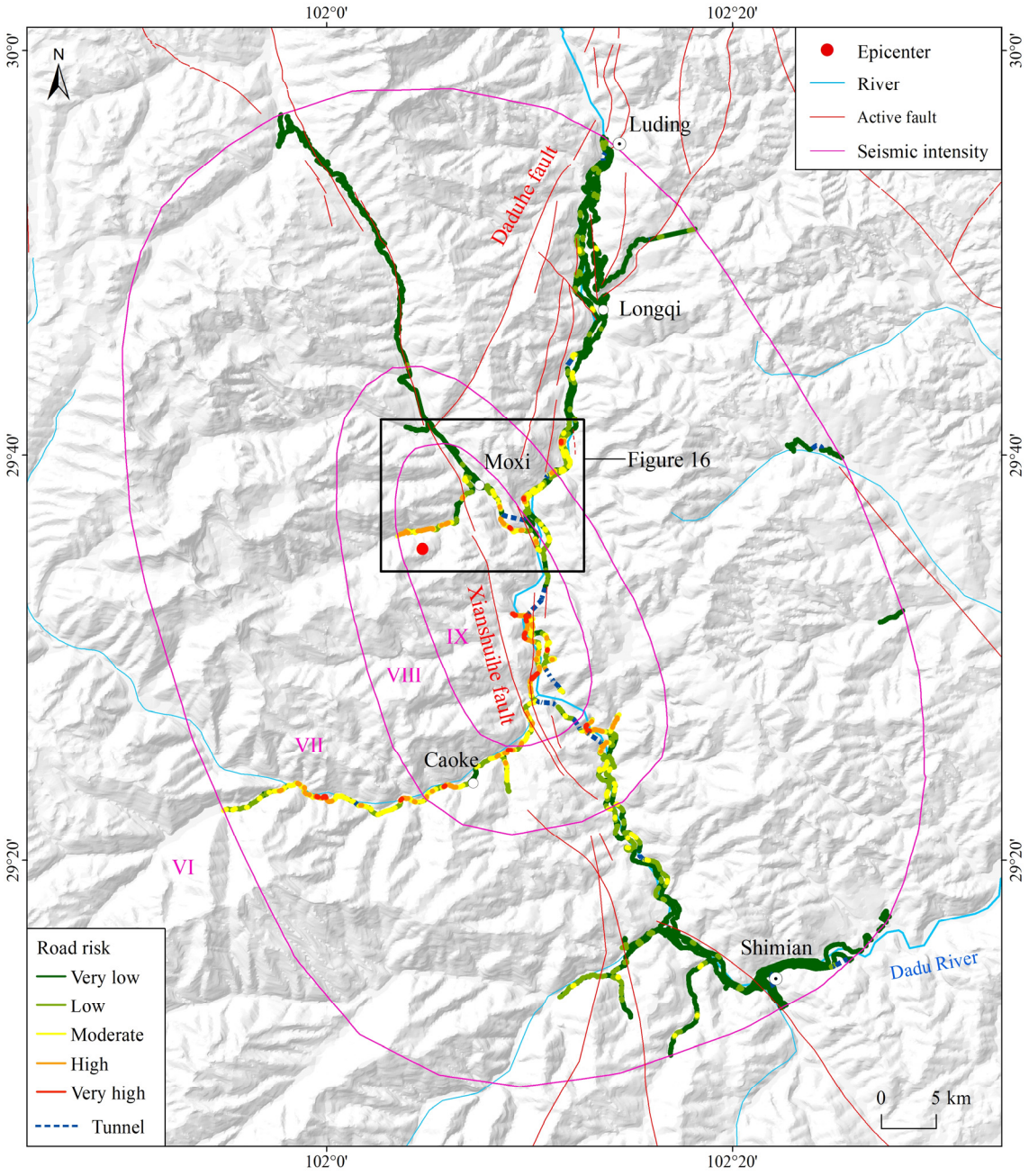


**Figure 15.** Seismic landslide risk posed to roads within the Luding earthquake area.

Moxi town is a tourist area with 7243 permanent residents and a large number of tourists. Based on the optimized seismic landslide hazard evaluation results, the linear road data, and the plane building data of the Moxi region near the epicenter were overlaid to assess the seismic landslide risk posed to roads and buildings, which was classified into five levels as very high, high, moderate, low, and very low (Figure 16). The tourist road leading to the Hailuogou scenic area, the provincial road spreading at the foot of the slopes along both banks of the Duda River, and the old road (Figure 17) leading to Moxi Town all face very high and high seismic landslide risk. The buildings on the Moxi platform are shielded from seismic landslides originating from the high and steep mountains due to the river valleys flanking both sides of the platform (Figure 5e,f). Conversely, the buildings situated at the feet of the slopes along both banks of the Duda River are exposed to an elevated risk of seismic landslides, necessitating thorough and careful consideration.

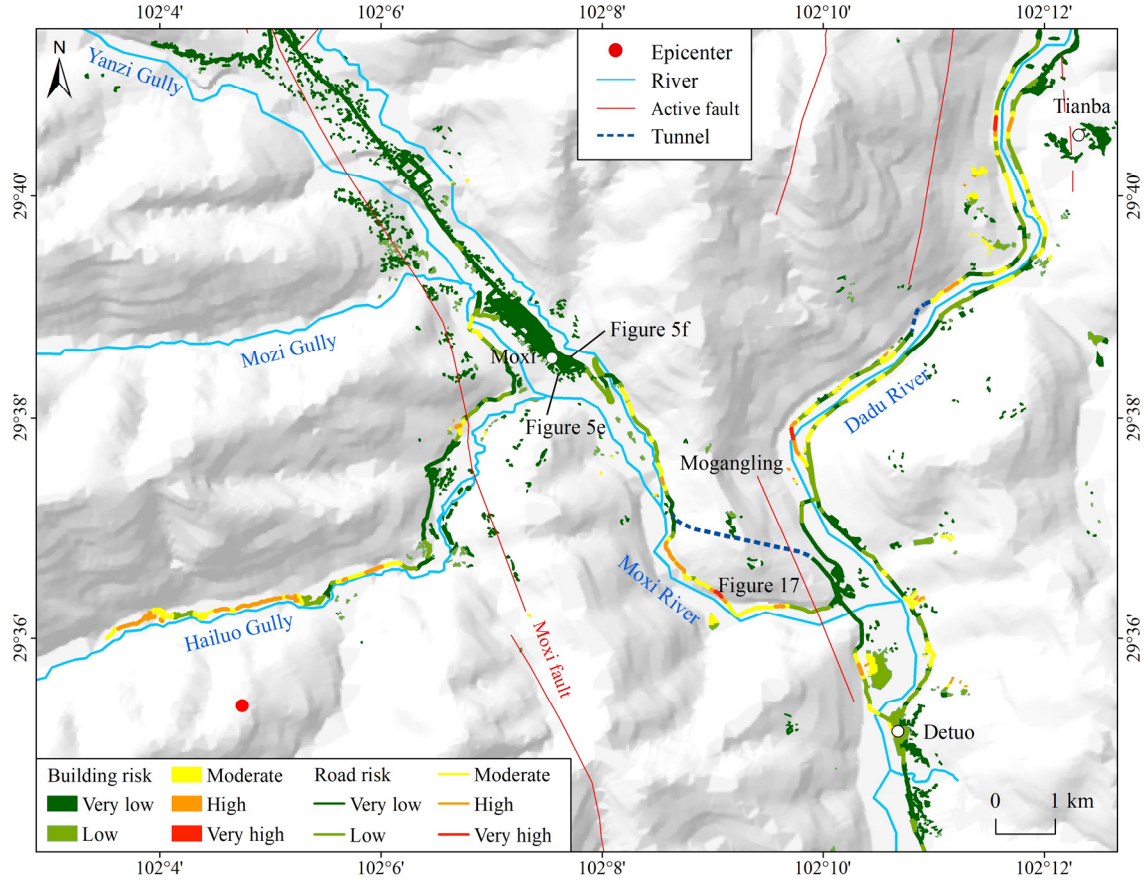


**Figure 16.** Seismic landslide risk posed to roads and buildings in the Moxi area.

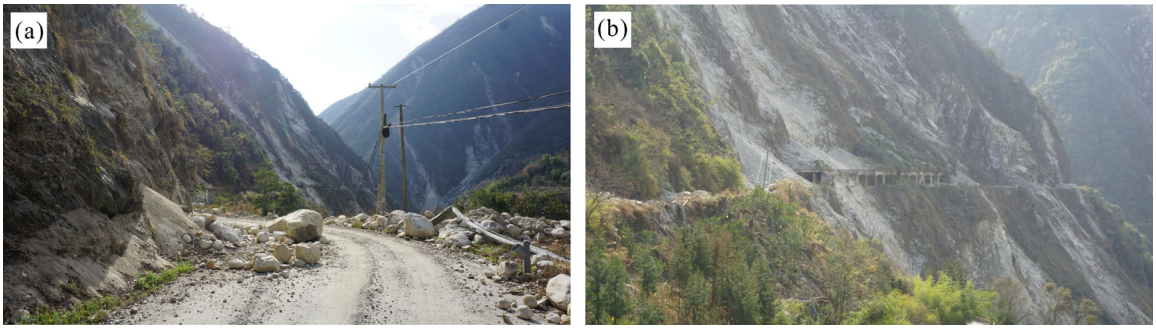


**Figure 17.** The representative Luding earthquake-induced destructive landslides. (**a**) Landslide block road. (**b**) Landslide damage road protection shed. These photos come from field survey in 2022 conducted by the author of this paper.

## 5. Discussions

The traditional models and methods only identify the landslide hazard source points and do not consider its dynamic runout process after the landslide instability, which underestimates the seismic landslide hazard. Around this issue, the joint Newmark–Runout model based on landslide dynamic runout is proposed in this study to enhance the precision of seismic landslide hazard evaluation. It must be stated that, in addition to the Newmark model, the static seismic landslide hazard can also be achieved by using an expert-experience scoring method, artificial neural network [8], logistic regression [10], and other machine-learning methods. In addition to the Rockfall model, discrete-element methods, Massflow, RAMMS, and other numerical models can also be utilized to conduct the dynamic runout simulation of a complex rock mass. But, these models and methods need to establish an

independent numerical engineering geological model for each landslide, which requires a lot of work and calculation.

The number of seismic monitoring stations within the Luding earthquake area is limited, resulting in low density and uneven distribution. Consequently, the simulated PGAs derived from the seismic monitoring station data are biased [33], which inevitably leads to a bias in seismic landslide risk identification. The Newmark model will also be compatible with Arias intensity and other ground-motion parameters [15], which can be derived from a comprehensive analysis of seismogenic fault characteristics and focal mechanism solutions. Subsequently, further comparative research on seismic landslide risk identification should be conducted.

The essence of the simplified Newmark model, grounded in statistical principles, lies in calculating the landslide occurrence probability based on slope displacement. In this study, a statistical empirical relationship is employed to calculate seismic slope displacement [30]. Subsequently, the functional relationship between landslide occurrence probability and seismic slope displacement is statistically fitted using the Luding earthquake-induced landslides as the samples, thereby partly enhancing the traditional Newmark model. Subsequently, the more precise seismic slope displacement can be derived through the quadratic integration of seismic motion acceleration over time, thereby further enhancing the evaluation accuracy.

The steep mountains exhibit a pronounced topographic amplification effect on seismic motion, particularly at the mountain summits. In this study, seismic landslide evaluation works are conducted at a regional scale without considering the topographic amplification effect of seismic motion. Consequently, considering this factor, the current seismic landslide evaluation results are relatively conservative. In this study, the seismic landslide risk identification is mainly aimed at earthquake relief and emergency rescue, not considering the value of roads and buildings, but only considering the damage degree of roads and buildings, especially the congestion degree of roads.

In mountainous and gorge complex geomorphological areas, landslides triggered by earthquakes not only cause damage in the source zone but also often cause greater damage in the sliding zone and debris accumulation zone. Therefore, the movement process of landslides should be considered an important factor in seismic landslide hazard evaluation and seismic landslide risk identification. The proposed joint Newmark–Runout model and research approach have a certain universal significance in seismic landslide risk identification in similar areas.

## 6. Conclusions

The number of landslides induced by the Luding earthquake is substantial, although their scale tends to be small, with a predominant distribution in areas exhibiting seismic intensities of VII and above. Active faults, topography, lithology, and river gully significantly control the spatial distribution of these landslides. The area with the largest frequency density of landslides is 90–110 $m^2$.

A joint Newmark–Runout model based on landslide dynamic runout is proposed to optimize the seismic landslide hazard and enhance its precision. The functional relationship between landslide occurrence probability and slope displacement is statistically fitted, which partially refines the calculation steps of the simplified Newmark model and renders it more suitable for the geological setting of the southern Xianshuihe fault zone.

The identification of the seismic landslide risk posed to roads and buildings at a regional scale has been completed. The lengths of the roads facing very high and high seismic landslide risk are 3.36 km and 15.66 km, respectively, being primarily distributed between Moxi Town and Caoke Town. The buildings on the Moxi platform are subject to lower seismic landslide risk, while those situated at the feet of the slopes along both banks of the Duda River are exposed to an elevated seismic landslide risk.

This study only considered the movement trajectory lines of the rock masses but did not take into account the thickness of rock mass accumulation. Other detailed factors, such as road grade and the number of people living in houses, were not considered. These detailed

factors need to be further studied. The static and dynamic seismic landslide hazard levels were fused together with equal weights, and their respective weight values are worthy of further exploration.

**Author Contributions:** Conceptualization, Y.W.; Methodology, Z.Y.; Validation, C.G.; Formal analysis, C.G.; Investigation, Z.Y.; Data curation, X.M.; Writing—original draft, Z.Y.; Writing—review & editing, Y.W.; Visualization, C.G. and X.M.; Funding acquisition, Z.Y. and Y.W. All authors have read and agreed to the published version of the manuscript.

**Funding:** This study was supported by the National Natural Science Foundation of China (Grant NO. 42277180), the Science and Technology Plan Project of Linzhi, Xizang (Grant NO. SYQ2024-12), the Opening Foundation of the State Key Laboratory of Resources and Environmental Information System, and the China Geological Survey Project (Grant NO. DD20221816).

**Data Availability Statement:** The orthophoto images are available in the Mountain Science Data Center at https://www.msdc.ac.cn/#/, accessed on 7 September 2022. The landslide data are available at https://link.springer.com/article/10.1007/s11629-022-7772-0, accessed on 28 March 2023, and https://doi.org/10.1016/j.eqrea.2022.100181, accessed on 1 January 2023. The PGAs data are available in the published literature [30]. The ARSTER GDEM data are available at https://search.asf.alaska.edu/#/, accessed on 7 September 2022.

**Conflicts of Interest:** The authors declare no conflict of interest.

## References

1. Parsons, T.; Ji, C.; Kirby, E. Stress changes from the 2008 Wenchuan earthquake and increased hazard in the Sichuan basin. *Nature* **2009**, *454*, 509–510. [CrossRef] [PubMed]
2. Kamp, U.; Growley, B.J.; Khattak, G.A.; Owen, L.A. GIS-based landslide susceptibility mapping for the 2005 Kashmir earthquake region. *Geomorphology* **2008**, *101*, 631–642. [CrossRef]
3. Valagussa, A.; Frattini, P.; Valbuzzi, E.; Crosta, G.B. Role of landslides on the volume balance of the Nepal 2015 earthquake sequence. *Sci. Rep.* **2021**, *11*, 3434. [CrossRef] [PubMed]
4. Bai, S.B.; Wang, J.; Zhang, Z.G.; Cheng, C. Combined landslide susceptibility mapping after Wenchuan earthquake at the Zhouqu segment in the Bailongjiang Basin, China. *Catena* **2012**, *99*, 18–25. [CrossRef]
5. Khattak, G.A.; Owen, L.A.; Kamp, U.; Harp, E.L. Evolution of earthquake-triggered landslides in the Kashmir Himalaya, northern Pakistan. *Geomorphology* **2010**, *115*, 102–108. [CrossRef]
6. Martino, S.; Mugnozza, G.S. The role of the seismic trigger in the Calitri landslide (Italy): Historical reconstruction and dynamic analysis. *Soil Dyn. Earthq. Eng.* **2005**, *25*, 933–950. [CrossRef]
7. Zhou, J.W.; Cui, P.; Fang, H. Dynamic process analysis for the formation of Yangjiagou landslide-dammed lake triggered by the Wenchuan earthquake, China. *Landslides* **2013**, *10*, 331–342. [CrossRef]
8. Yilmaz, I. Comparison of landslide susceptibility mapping methodologies for Koyulhisar, Turkey: Conditional probability, logistic regression, artificial neural networks, and support vector machine. *Environ. Earth Sci.* **2010**, *61*, 821–836. [CrossRef]
9. Song, Y.Q.; Gong, J.H.; Gao, S.; Wang, D.C.; Cui, T.J.; Li, Y.; Wei, B.Q. Susceptibility assessment of earthquake-induced landslides using Bayesian network: A case study in Beichuan, China. *Comput. Geosci.* **2012**, *42*, 189–199. [CrossRef]
10. Nefeslioglu, H.A.; Duman, T.Y.; Durmaz, S. Landslide susceptibility mapping for a part of tectonic Kelkit Valley (Eastern Black Sea region of Turkey). *Geomorphology* **2006**, *94*, 401–418. [CrossRef]
11. Roccati, A.; Paliaga, G.; Luino, F.; Faccini, F.; Turconi, L. GIS-Based Landslide Susceptibility Mapping for Land Use Planning and Risk Assessment. *Land* **2021**, *10*, 162. [CrossRef]
12. Ullah, I.; Aslam, B.; Shah, S.H.I.A.; Tariq, A.; Qin, S.; Majeed, M.; Havenith, H.-B. An Integrated Approach of Machine Learning, Remote Sensing, and GIS Data for the Landslide Susceptibility Mapping. *Land* **2022**, *11*, 1265. [CrossRef]
13. Wilson, R.C.; Keefer, D.K. Dynamic analysis of a slope failure from the 6 August 1979 Coyote lake, California, earthquake. *Bull. Seismol. Soc. Am.* **1983**, *73*, 863–877. [CrossRef]
14. Miles, S.B.; Ho, C.L. Rigorous landslide hazard zonation using Newmark's method and stochastic ground motion simulation. *Soil Dyn. Earthq. Eng.* **1999**, *18*, 305–323. [CrossRef]
15. Chousianitis, K.; Del, G.V.; Kalogeras, I.G.A. Predictive model of Arias intensity and Newmark displacement for regional scale evaluation of earthquake-induced landslide hazard in Greece. *Soil Dyn. Earthq. Eng.* **2014**, *65*, 11–29. [CrossRef]
16. Pareek, N.; Pal, S.; Kaynia, A.M.; Sharma, M.L. Empirical-based seismically induced slope displacements in a geographic information system environment: A case study. *Georisk Assess. Manag. Risk Eng. Syst. Geohazards* **2014**, *8*, 258–268. [CrossRef]
17. Rathje, E.M.; Sayg, G. Probabilistic seismic hazard analysis for the sliding displacement of slopes: Scalar and vector approaches. *J. Geotech. Geoenviron.* **2008**, *134*, 804–814. [CrossRef]
18. Nowicki, M.A.; Wald, D.J.; Hamburger, M.W.; Hearne, M.; Thompson, E.M. Development of a globally applicable model for near real-time prediction of seismically induced landslides. *Eng. Geol.* **2014**, *173*, 54–65. [CrossRef]

19. Ke, K.; Zhang, Y.; Zhang, J.; Chen, Y.; Wu, C.; Nie, Z.; Wu, J. Risk Assessment of Earthquake–Landslide Hazard Chain Based on CF-SVM and Newmark Model—Using Changbai Mountain as an Example. *Land* **2023**, *12*, 696. [CrossRef]
20. Yue, X.L.; Wu, S.H.; Yin, Y.H.; Gao, J.B.; Zheng, J.Y. Risk Identification of Seismic Landslides by Joint Newmark and RockFall Analyst Models: A Case Study of Roads Affected by the Jiuzhaigou Earthquake. *Int. J. Disast. Risk Sci.* **2018**, *9*, 392–406. [CrossRef]
21. Dai, L.X.; Fan, X.M.; Wang, X.; Fang, C.Y.; Zou, C.B.; Tang, X.C.; Wei, Z.L.; Xia, M.Y.; Wang, D.; Xu, Q. Coseismic landslides triggered by the 2022 Luding Ms6.8 earthquake, China. *Landslides* **2023**, *20*, 1277–1292. [CrossRef]
22. Huang, Y.D.; Xie, C.C.; Li, T.; Xu, C.; He, X.L.; Shao, X.Y.; Xu, X.W.; Zhan, T.; Chen, Z.N. An open-accessed inventory of landslides triggered by the Ms 6.8 Luding earthquake, China on September 5, 2022. *Earthq. Res. Adv.* **2023**, *3*, 100181. [CrossRef]
23. Zhang, J.Q.; Yang, Z.J.; Meng, Q.K.; Wang, J.; Kai-Heng, H.U.; Yong-Gang, G.E.; Feng-Huan, S.U.; Zhao, B.; Zhang, B.; Jiang, N. Distribution Patterns of Landslides Triggered by the 2022 Ms 6.8 Luding Earthquake, Sichuan, China. *J. Mt. Sci.* **2023**, *20*, 607–623. [CrossRef]
24. Guo, C.B.; Li, C.H.; Yang, Z.H.; Ni, J.W.; Zhong, N.; Wang, M.; Yan, Y.Q.; Song, D.G.; Zhang, Y.N.; Zhang, X.B. Characterization and spatial analysis of coseismic landslides triggered by the Luding Ms 6.8 earthquake in the Xianshuihe fault zone, southwest China. *J. Mt. Sci.* **2024**, *21*, 160–181. [CrossRef]
25. Shao, X.Y.; Ma, S.Y.; Xu, C.; Xie, C.C.; Li, T.; Huang, Y.D.; Huang, Y.; Xiao, Z.K. Landslides triggered by the 2022 Ms. 6.8 Luding strike-slip earthquake: An update. *Eng. Geol.* **2024**, *335*, 107536. [CrossRef]
26. Newmark, N.M. Effects of earthquakes on dams and embankments. *Geotechnique* **1965**, *15*, 139–160. [CrossRef]
27. Jibson, R.W. Predicting earthquake-induced landslide displacements using Newmark's sliding block analysis. *Transpor. Res. Rec.* **1993**, *1411*, 9–17.
28. Roberto, R. Seismically induced landslide displacements: A predictive model. *Eng. Geol.* **2000**, *58*, 337–351. [CrossRef]
29. Jibson, R.W.; Harp, E.L.; Michael, J.A. A method for producing digital probabilistic seismic landslide hazard maps. *Eng. Geol.* **2000**, *58*, 271–289. [CrossRef]
30. Jibson, R.W. Regression models for estimating coseismic landslide displacement. *Eng. Geol.* **2007**, *91*, 209–218. [CrossRef]
31. Lan, H.X.; Martin, C.D.; Lim, C.H. Rockfall analyst: A GIS extension for three-dimensional and spatially distributed rockfall hazard modeling. *Comput. Geosci.* **2007**, *33*, 262–279. [CrossRef]
32. Lan, H.X.; Martin, C.D.; Zhou, C.H.; Lim, C.H. Rockfall hazard analysis using LiDAR and spatial modeling. *Geomorphology* **2010**, *118*, 213–223. [CrossRef]
33. Wang, Y.J.; Zhang, L.F.; Sun, X.D.; Zhao, Y.N.; Li, J.G. Near-field strong motion simulation of the 2022 Luding Ms6.8 earthquake in Sichuan province. *J. Geod. Geodyn.* **2023**, *43*, 441–446+516, (In Chinese with English Abstract) [CrossRef]
34. Fan, X.M.; Scaringi, G.; Korup, O.; West, A.J.; Westen, C.J.V.; Tanyas, H.; Hovius, N.; Hales, T.C.; Jibson, R.W.; Allstadt, K.E.; et al. Earthquake-Induced Chains of Geologic Hazards: Patterns, Mechanisms, and Impacts. *Rev. Geophy.* **2019**, *57*, 421–503. [CrossRef]
35. Bai, M.K.; Chevalier, M.L.; Pan, J.W.; Replumaz, A.; Leloup, P.H.; Métois, M.; Li, H.B. Southeastward increase of the late Quaternary slip-rate of the Xianshuihe fault, eastern Tibet. Geodynamic and seismic hazard implications. *Earth Planet. Sci. Lett.* **2018**, *485*, 19–31. [CrossRef]
36. Zhang, P.Z. A review on active tectonics and deep crustal processes of the Western Sichuan region, eastern margin of the Tibetan Plateau. *Tectonophysics* **2013**, *584*, 7–22. [CrossRef]
37. Wang, Y.Z.; Wang, M.; Shen, Z.K. Block-like versus distributed crustal deformation around the northeastern Tibetan plateau. *J. Asian Earth Sci.* **2017**, *140*, 31–47. [CrossRef]
38. Allen, C.R.; Luo, Z.L.; Qian, H.; Wen, X.Z.; Zhou, H.W.; Huang, W.S. Field study of a highly active fault zone: The Xianshuihe fault of southwestern China. *Geol. Soc. Am. Bull.* **1991**, *103*, 1178–1199. [CrossRef]
39. Zhang, Y.S.; Yang, Z.H.; Guo, C.B.; Wang, T.; Wang, D.H.; Du, G.L. Predicting landslide scenes under potential earthquake scenarios in the Xianshuihe fault zone, Southwest China. *J. Mt. Sci.* **2017**, *14*, 1262–1278. [CrossRef]
40. Chen, G.H.; Xu, X.W.; Wen, X.Z.; Chen, Y. Late Quaternary slip-rates and slip partitioning on the southeastern Xianshuihe fault system, eastern Tibetan Plateau. *Acta. Geol. Sin-Engl.* **2016**, *90*, 537–554. [CrossRef]
41. *GB/T 17742-2020*; The Chinese Seismic Intensity Scale. Standard Press of China: Beijing, China, 2020.
42. Liu, X.M.; Su, P.C.; Li, Y.; Xia, Z.X.; Ma, S.Y.; Xu, R.; Lu, Y. Spatial distribution of landslide shape induced by Luding Ms6.8 earthquake, Sichuan, China: Case study of the Moxi Town. *Landslides* **2023**, *20*, 1667–1678. [CrossRef]
43. Hua, J.X.; Zheng, J.G.; Wang, D.L. *Engineering Geology Handbook (Fifth Edition) of China*; China Architecture and Building Press: Beijing, China, 2018; (In Chinese with English Abstract)
44. *GB/T 50218-2014*; Standard for Engineering Classification of Rock Mass of China. China Planning Press: Beijing, China, 2014.
45. Yang, Z.H.; Guo, C.B.; Wu, R.A.; Shao, W.W.; Yu, P.F.; Li, C.H. Potential seismic landslide hazard and engineering effect in the Ya'an-Linzhi section of the Sichuan-Tibet transportation corridor, China. *China Geol.* **2023**, *6*, 228–240. [CrossRef]


**Disclaimer/Publisher's Note:** The statements, opinions and data contained in all publications are solely those of the individual author(s) and contributor(s) and not of MDPI and/or the editor(s). MDPI and/or the editor(s) disclaim responsibility for any injury to people or property resulting from any ideas, methods, instructions or products referred to in the content.